Journal of Health Sciences

RESEARCH ARTICLE Open Access

Accuracy of volumetric modulated arc radiotherapy of the thoracic region based on HyperSight imager

Goran Kolarević[1,2,3,4], Tatjana Ignjatić[2,3], Dejan Ignjatić[2], Elena Omerović[2], Marija Brkić[2], Amel Kamenjaš[2], Samir Karamujić[2], Dejan Ćazić[2], Aleksandar Kostovski[1,2], Goran Marošević[1,2,5]

[1]Department of Radiation Therapy, Medikol Polyclinic, Zagreb, Croatia, [2]Department of Radiation Therapy, Medikol Salinea, Živinice, Bosnia and Herzegovina, [3]Department of Medical Physics, Faculty of Medicine, University of Banja Luka, Banja Luka, Bosnia and Herzegovina, [4]Department of Physics, Faculty of Natural Sciences and Mathematics, University of Banja Luka, Banja Luka, Bosnia and Herzegovina, [5]Department of Oncology and Radiotherapy, Faculty of Medicine, University of Banja Luka, Banja Luka, Bosnia and Herzegovina

ABSTRACT

Introduction: This study evaluated the accuracy of various cone-beam computed tomography (CBCT) reconstruction modalities, specifically the HyperSight (HS) detector, in comparison to standard computed tomography (CT) simulation for potential use in online adaptive radiotherapy. The research focused on the Hounsfield Unit (HU) to relative electron density (RED) conversion and its subsequent impact on volumetric modulated arc therapy (VMAT) dose calculations.

Methods: Two tissue-equivalent phantoms, the advanced electron density and the CIRS Thorax phantom, were utilized. Imaging was performed on a SOMATOM go.Open Pro CT simulator and a Varian TrueBeam medical linear accelerator using CBCT, HS-CBCT, HS-iterative CBCT (iCBCT) and HS-iCBCT metal artifact reduction protocols. Calibration curves (HU-RED) were generated for two regions: RED <1.2 and 1.2≤ RED <1.8. VMAT plans (6 MV) were created in the Eclipse 18.1 treatment planning system (TPS), using an anisotropic analytical algorithm (AAA) and Acuros XB algorithm. Absolute dose measurements were conducted using an SNC125c ionization chamber and compared with TPS-calculated doses.

Results: In the soft-tissue region (RED <1.2), all imaging modalities showed an excellent linear correlation with CT ($r > 0.998$), with HU deviations within ± 30 HU. In the high-density region (1.2 ≤ RED < 1.8), HS-CBCT demonstrated superior stability with the lowest root mean square error, 62.88 HU. Dosimetric results showed that 96.7% of all measurement points met the ± 3–4% agreement criteria. For the AAA algorithm, HS-iCBCT exhibited the highest precision (standard deviation = 0.59) and the lowest mean absolute error. The Friedman test confirmed a statistically significant difference between modalities ($p < 0.05$), with HS-iCBCT showing the most consistent performance.

Conclusion: Both HS-CBCT and HS-iCBCT provide highly accurate HU-RED conversions and reliable dosimetric results for RED < 1.8.

Keywords: Cone-beam computed tomography; HyperSight; relative electron density; volumetric modulated arc therapy; dosimetry; adaptive radiotherapy

INTRODUCTION

Treatment planning within external beam radiation therapy has, for nearly five decades, relied on the synergy between computed tomography (CT) imaging and sophisticated treatment planning systems (TPS). The clinical goal remains a near-ideal match between the TPS-calculated isodose distribution to the patient and delivery via a medical linear accelerator (LINAC). The fidelity of this process is strongly related to the accuracy of the input commissioned LINAC and CT data and the specific dose calculation algorithms used. The basic value for this is the Hounsfield Unit (HU) that the CT simulator provides for each voxel, a value determined by the energy of the photon beam and the effective atomic number (Z) of the tissue. To compensate for the significant spectral differences between the kilovolt photon beams used in the CT simulation and the megavolt LINAC beams, a calibration-based approach was implemented. This involves the use of CT to relative electron density (RED) conversion curves, which translate HU into physical properties such as electron density or mass density (MD). By adopting this conversion framework, the RED remains invariant with respect to the energy spectrum of the incident photon. It is a well-recognized phenomenon in medical physics that these conversion curves for high-density materials (>300 HU) exhibit significant sensitivity to variations in X-ray tube voltage (1).

A milestone in modern radiotherapy (RT) is the integration of on-board imaging directly onto the LINAC gantry, most

*Corresponding author: Goran Kolarević, Department for Radiation Therapy, Medikol Polyclinic, Voćarska Cesta 106, 10000 Zagreb, Croatia. E-mail: goran.kolarevic@medikol.hr

Submitted: 10 April 2026/Accepted: 02 July 2026

DOI: https://doi.org/10.17532/jhsci.2026.3054

UNIVERSITY OF SARAJEVO FACULTY OF HEALTH STUDIES

© 2026 Goran Kolarević, *et al.*; licensee University of Sarajevo - Faculty of Health Studies. This is an Open Access article distributed under the terms of the Creative Commons Attribution License (https://creativecommons.org/licenses/by/4.0/), which permits unrestricted use, distribution, and reproduction in any medium, provided the original work is properly cited.

notably in the form of cone-beam CT (CBCT). While primarily used for improving setup precision, CBCT has laid the groundwork for adaptive RT (ART) by potentially bypassing the need for repeated conventional CT simulations. However, traditional CBCT often suffers from degraded image quality characterized by high noise and significant photon scatter, leading to HU inconsistencies when compared to fan-beam CT. These limitations are largely attributed to the beam scatter, hardening, and acquisition geometry, while Feldkamp-Davis-Kress (FDK) reconstruction further amplifies these effects. FDK filtered back-projection algorithm, which is notoriously susceptible to artifacts in dense anatomical regions (2,3). To address these challenges, HyperSight (HS) technology (Varian Medical Systems Inc., Palo Alto, CA, USA) has been introduced to facilitate online ART (oART). This system incorporates an expanded field of view (FOV), an optimized detector, and accelerated gantry rotation. More importantly, HS utilizes a sophisticated iterative reconstruction algorithm, iterative CBCT (iCBCT) coupled with a grid-based Boltzmann–Solver for scatter correction, which is designed to reduce a substantial reduction in noise and artifacts compared to FDK-based methods. Such technical refinements are expected to enhance the reliability of dose calculations derived directly from HS-iCBCT datasets (4).

The clinical implementation of daily image-guided RT allows for the reduction of clinical target volume to planning target volume (PTV) margins by minimizing interfraction positioning errors. Furthermore, daily imaging serves as a positioning verification and assessment of anatomical changes for identifying anatomical shifts that necessitate plan adaptation. Transitioning to CBCT-based planning would not only eliminate the logistical burden of repeated CT simulations but also significantly optimize the clinical workflow. The current workflow in RT suggests a shift where conventional CT simulators may eventually be superseded by advanced on-board CBCT imaging for primary treatment planning (5).

The primary objective of this HU-RED calibration accuracy and its impact on dose calculation is to evaluate potential discrepancies between HU-RED calibration curves generated from multiple imaging modalities: a reference CT simulator, standard CBCT, HS-CBCT, HS-iCBCT, and HS-iCBCT with metal artifact reduction (MAR), all maintained at consistent tube voltages. By identifying which modalities most closely align with the reference CT, this study aims to assess the accuracy of dose calculations within the Eclipse 18.1 TPS (Varian Medical Systems Inc., Palo Alto, CA, USA). The evaluation focuses on the delivery of volumetrically modulated arc therapy (VMAT), photon beam energy of 6 MV, and comparing isodose distributions obtained using the analytical anisotropic algorithm (AAA) and Acuros XB, to delivered dose measurements on the LINAC. All experimental work was performed using a heterogeneous thorax phantom to replicate the complexities of lung cancer dosimetry.

METHODS

In this study, we investigated the agreement between the measured dose at the LINAC and the dose calculated in the TPS for different imaging modalities. To systematically assess the impact of different imaging modalities and their associated calibration and conversion curves, a methodological framework based on standardized principles was implemented. Continuity of the research process was maintained using standardized protocols, which guaranteed repeatability of measurements and minimized subjective differences during data collection and processing.

Data acquisition was conducted using the TrueBeam (TB) LINAC, version 4.1 (Varian Medical Systems Inc., Palo Alto, CA, USA), utilizing a gantry rotation speed of 1.5 rotations/min, which equates to an angular velocity of 9°/s. Under these parameters, a standard half-fan body scan was completed in approximately 40 s. The system integrated the HS imaging panel, a high-efficiency detector offering a 43 × 43 cm² active area (6). This configuration supports a 48.5 cm scan diameter, with the capacity for an extended FOV reconstruction reaching up to 70 cm.

Standardized thorax scanning protocol was implemented across three distinct imaging environments: the reference CT simulator SOMATOM go.Open Pro (Siemens Healthineers, Erlangen, DE) (7), the HS-equipped TB LINAC (8), and a secondary TB LINAC without HS technology.

For the generation of HU-to-RED curves, the advanced electron density (AED) phantom (Sun Nuclear, Melbourne, FL, USA) was used. This tissue-equivalent system is designed to facilitate an accurate HU to RED conversion curve based on the CT and CBCT images. The phantom's architecture comprises two plastic water disks (Figure 1), which, when integrated, replicate the dimensions of a human pelvis (40 cm horizontal diameter), whereas the central component serves as a surrogate for the human head (20 cm diameter). The assembly incorporates 15 distinct tissue-equivalent inserts with precisely defined RED and MD (Table 1). These inserts can be strategically configured across 16 available positions to simulate various anatomical heterogeneities (9).

In addition to the AED phantom, a CIRS Thorax phantom (Sun Nuclear, Melbourne, FL, USA) was used to

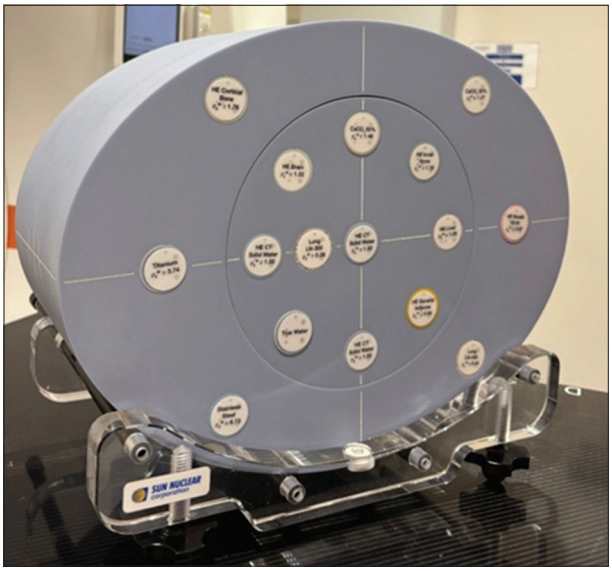

FIGURE 1. Advanced electron density phantom.

TABLE 1. AED phantom, relative electron density data

AED-materials	RED
Lung LN-300	0.314
Lung LN-450	0.452
HE gen adipose	0.948
HE breast 50:50	0.977
True water insert	1.000
HE CT solid water	1.001
HE brain	1.026
HE liver	1.055
HE inner bone	1.167
CB_2+30% $CaCO_3$	1.265
CB_2+50% $CaCO_3$	1.464
HE cortical bone	1.773
Aluminium core	2.360
Titanium core	3.740
Stainless steel core	6.730

represent the anatomical and density characteristics of the average human thorax. With dimensions of 29 cm × 30 cm × 20 cm, this heterogeneous phantom is constructed from epoxy materials, including plastic water (RED = 1.000), lung (RED = 0.207), and bone (RED = 1.506). The phantom is equipped with 10 dedicated cylindrical inserts (Figure 2) specifically engineered to accommodate an ionization chamber, thereby facilitating high-precision absolute dose measurements within different simulated tissue environments (10).

The initial scanning of both phantoms was performed on the SOMATOM go.Open Pro CT simulator, utilizing its 85 cm gantry aperture. A standardized clinical thorax protocol was implemented, employing a tube voltage of 120 kV and a total current-time product of 964 mAs. Image reconstruction was executed with a 512 × 512 matrix, a standard filter, a slice thickness of 1.25 mm, and a rotation time of 1 s.

Comparative datasets were acquired on the TB platforms across multiple imaging modalities, including standard CBCT, HS-CBCT, HS-iCBCT, and HS-iCBCT MAR. These scans utilized a pelvis protocol (125 kV, 1060 mAs, half-fan). To establish the calibration-conversion curves RED = f(HU), the AED phantom was scanned with tissue-equivalent cylindrical inserts (Table 1) distributed in randomized positions throughout the phantom body to account for potential positional dependencies.

The resulting image datasets were analyzed within the Eclipse 18.1 RT TPS. To determine the HU values of each material, the mean HU and standard deviation (SD) were derived from three independent readings on different slices of the image, thereby accounting for stochastic variations in the scan data. To ensure the integrity of the HU measurements and minimize partial volume effects, a square region of interest (ROI) with sides of 1 cm was defined within each inset. This ROI was carefully positioned to exclude the peripheral edge zones of the inserts (Figure 3). The generated conversion curves were categorized and evaluated across two distinct RED regions: RED < 1.2 and RED ≥ 1.2 (1,11). All derived curves (CT, CBCT, HS-CBCT, HS-iCBCT, and HS-iCBCT MAR) were subsequently integrated into the TPS for dosimetric evaluation. For body region comparison, a threshold of ± 30 HU (6) at any

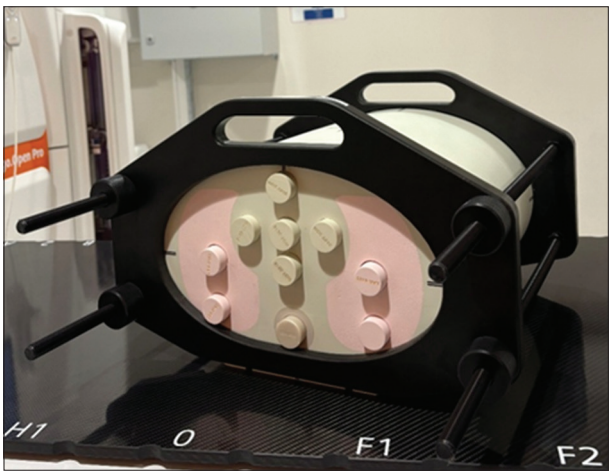

FIGURE 2. CIRS Thorax phantom.

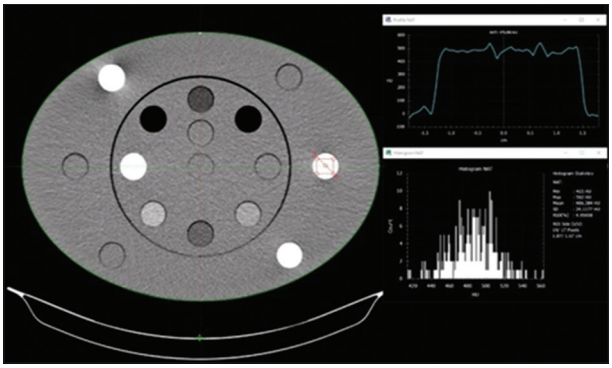

FIGURE 3. Axial computed tomography scan of an advanced electron density pelvis phantom with region of interest analysis (histogram and Hounsfield unit profile).

specific RED value was established as a criterion for clinical acceptability between curves.

For the phase of determining the difference between measured and TPS planned doses, VMAT plans were created within the Eclipse 18.1 TPS platform, using 6 MV photon beams. To assess the impact of different imaging modalities on dose calculation accuracy, individual plans were created using CT, HS-CBCT, and HS-iCBCT datasets. Each plan was calculated separately with its specific corresponding calibration and conversion curve RED = f(HU). The dose distribution for each imaging modality was determined using two different calculation algorithms, AAA and Acuros XB.

The end product of the planning is a precise volumetric isodose distribution throughout the phantom volume. Furthermore, the TPS allows us to obtain absolute dose values at defined points within different tissue equivalent components of the CIRS Thorax phantom, Figure 4 (12). Comprehensive geometric and dosimetric specifications for these clinical plans, along with the prescribed dose constraints for organs at risk, are detailed in Table 2 (13). On the transverse scan of the CIRS Thorax phantom, contours were made of the PTV located in soft and lung tissue, the heart located in soft tissue, the left and right lung (total lung), and the spinal canal (bone). All contours were expanded 8 cm cranio-caudally (13).Physical measurements were performed on a Varian TB LINAC equipped with a Millennium 120 multi-leaf collimator. A SNC125c ionization chamber (Sun Nuclear, Melbourne, FL, USA) with an active volume of

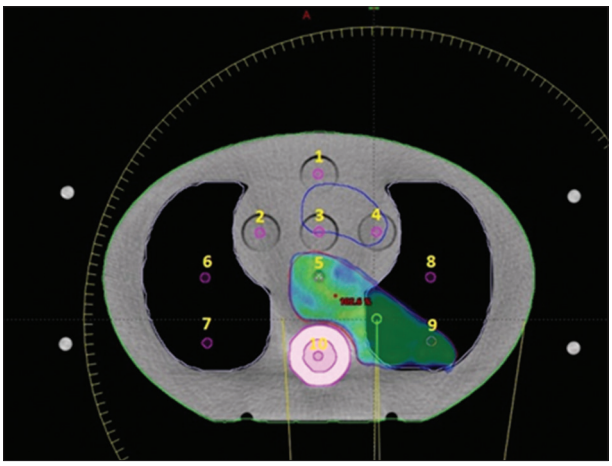

FIGURE 4. Volumetrically modulated arc therapy radiotherapy plan with beam geometry and isodose distributions on CIRS Thorax phantom with inserts for the soft tissue (1-5), lungs (6-9) and bone (10).

TABLE 2. Geometric parameters of VMAT RT plan, with dose limits for OAR

Clinical VMAT RT plan
Source-to-axis distance technique 1 full arc
Colimator-30°, Gantry: 181-179°, clockwise
Deliver 2 Gy to PTV (100% at target mean)
Dose constraints for OAR:
Spinal cord D_{max}<75% of the prescribed dose
Total lung $D_{20\%}$ <35%
Heart D_{max}<55% of the prescribed dose
Measurement points: 1-10

OAR: Online adaptive radiotherapy, PTV: Planning target volume, VMAT: Volumetrically modulated arc therapy, RT: Radiotherapy

0.108 cm³ was used to measure the absolute dose at specific measurement positions within the CIRS Thorax phantom for comparison with values calculated by TPS. Data acquisition was managed using a PC Electrometer (Sun Nuclear, Melbourne, FL, USA) interfaced with SunDOSE software. To ensure metrological traceability and accuracy, both the ionization chamber and the electrometer had undergone prior calibration at a secondary standard dosimetry laboratory. The determination of the absorbed dose at all specified measurement points was performed in strict accordance with the IAEA TRS-398 international dosimetry protocol.

A statistical framework was implemented to evaluate the fidelity of the calibration-conversion curves relative to the CT reference and to quantify the discrepancies in absolute dose measurements from the VMAT plans. The analytical assessment was based on the following metrics:

1. For each imaging modality, we calculated the difference of the read HU with respect to the HU from CT: $\Delta_i = HU_{method,i} - HU_{CT,i}$
   (where Δ represents the difference)
2. Mean difference (bias) $\Delta_{mean} = \frac{1}{n}\sum \Delta_i$
   (where n is the number of measurement points)
3. Mean absolute error $MAE = \frac{1}{n}\sum |\Delta_i|$
4. SD $SD = \sqrt{\frac{\sum(\Delta_i - \Delta_{mean})^2}{(n-1)}}$
5. Root mean square error $RMSE = \sqrt{\frac{\sum \Delta_i^2}{n}}$
   (gives the total deviation of the entire curve from the CT curve)
6. Maximum deviation $max\,|\Delta_i|$
   (shows the "worst" point)
7. Bivariate correlations, Pearson correlation coefficients
   $r = correlation\ (HU_i, HU_{CT})$
   (chosen level of significance α used to test the hypothesis, α = 0.05)
8. The Friedman non-parametric (χ^2) statistical test to detect differences across three or more related groups.

Given the finite number of available measurement points within the CIRS Thorax phantom, a normalization procedure was implemented to facilitate a robust comparison between experimental and calculated data. The absolute dose values, both measured on the LINAC (D_{meas}) and calculated by the TPS (D_{cal}), were normalized to the dose measured at the reference point ($D_{meas,ref}$) for each case, 2 Gy median PTV dose (13). This approach minimizes potential systematic setup uncertainties and allows for a direct evaluation of dose distribution accuracy. The absolute dose discrepancy was subsequently determined using the following equation:

$$X\ (Gy) = [(D_{cal} - D_{meas})/D_{meas,ref})]$$

The clinical acceptability threshold for deviations in VMAT absolute doses was determined within a tolerance range of 3–4%. Quantitative data are presented as arithmetic means, supplemented with the appropriate SDs or confidence intervals to indicate the precision of the measurements. All statistical calculations and data processing were performed using the Statistical Package for the Social Sciences Statistics 18 software package (IBM Corp., Armonk, NY, USA).

RESULTS

A set of HU values for a wide range of tissue-equivalent materials within the AED pelvic phantom enabled the generation of HU-RED calibration datasets for each imaging modality tested. The experimentally derived HU values, along with their associated SD for materials of precisely defined RED, are shown in Table 3.

Calibration curves obtained from the AED phantom in the RED range 0 < RED < 1.8 are shown in Figure 5a. For values of RED ≥ 1.8, the curves differ drastically (Table 3), and we did not consider them statistically. The main reasons for this are the saturation and non-linearity (HU-RED ratio) of CT and CBCT systems. X-ray attenuation becomes extremely high, detectors can saturate, and small noise or artifacts give large changes in HU. The reason is also that different reconstruction algorithms use different imaging modalities, and each of them treats noise, metal artifacts, and high densities differently. A focused overview of the interval 1.2 ≤ RED < 1.8 is shown in Figure 5b, where pronounced differences between the imaging modalities are observed. This particular subregion has great clinical application, as it encompasses the RED spectrum characteristic of different cortical and trabecular bone tissues, which are crucial for accurate dose calculation in heterogeneous anatomical areas.

The degree of agreement between the investigated imaging modalities and the reference CT image was assessed

TABLE 3. Experimentally determined HU values and corresponding SD for various imaging modalities (CT, CBCT, HS-CBCT, HS-iCBCT, and HS-iCBCT MAR) utilizing the AED phantom

RED	CT		CBCT		HS-CBCT		HS-iCBCT		HS-iCBCT MAR	
	HU	SD	HU	SD	HU	SD	HU	SD	HU	SD
0.001	−1000	0	−1000	0	−1000	0	−1000	0	−1000	0
0.314	−658.1	28.8	−638.0	47.2	−659.4	14.6	−676.2	28.4	−683.5	33.4
0.452	−585.2	37.9	−557.2	44.9	−584.2	26.6	−575.0	42.5	−589.1	53.5
0.948	−68.3	18.5	−63.1	54.4	−54.4	21.1	−82.5	19.6	−85.2	27.8
0.977	−29.1	27.8	−25.0	48.8	−17.3	29.0	−48.4	20.6	−44.1	26.3
1.000	0	20.5	−1.0	53.0	−6.0	19.2	18.0	18.6	4.5	39.0
1.001	3.1	20.0	−3.8	48.9	0.9	21.1	20.0	22.4	4.2	20.7
1.026	36.2	23.8	40.0	50.0	49.5	18.6	26.0	21.7	27.0	32.2
1.055	58.1	24.3	57.1	56.0	58.1	24.2	24.7	22.0	28.7	33.0
1.167	305.3	29.2	301.0	48.1	345.5	17.4	333.8	22.4	335.2	31.2
1.265	458.1	23.3	409.3	63.2	391.3	33.5	457.7	27.2	483.1	38.8
1.464	839.1	33.1	795.0	64.5	778.8	19.5	865.9	39.5	891.2	48.7
1.773	1358.3	38.5	1190.0	74.6	1296.5	54.4	1494.0	51.6	1545.0	65.4
2.360	2050.0	43.1	1771.2	84.5	2044.5	70.0	2246.6	39.3	2302.0	61.1
3.740	7510.1	610.0	5240.5	478.7	5547.6	161.3	7000.0	0	3735.9	1043.0
6.730	14450.1	1167.0	5442.2	589.5	5777.7	748.1	7000.0	0	3131.4	1942.6

RED: Relative electron density, CT: Computed tomography, CBCT: Cone beam computed tomography, HS-CBCT: HyperSight cone beam computed tomography, MAR: Metal artifact reduction, HU: Hounsfield unit, SD: Standard deviation

TABLE 4. Statistical indices of agreement and Pearson correlation coefficients between the reference CT and alternative imaging modalities (CBCT, HS-CBCT, HS-iCBCT, and HS-iCBCT MAR) within the RED <1.2 interval

Imaging	Δ_{mean} (HU)	SD (HU)	RMSE (HU)	Max Δ_i	Pearson (*r*)	*p*-value
CBCT	4.81	10.86	11.37	27.82	0.9997	<0.001
HS-CBCT	7.08	13.70	14.80	40.51	0.9996	<0.001
HS-iCBCT	−2.15	20.06	19.15	33.29	0.9988	<0.001
HS-iCBCT MAR	−6.44	17.15	17.50	30.18	0.9992	<0.001

RED: Relative electron density, CT: Computed tomography, CBCT: Cone beam computed tomography, HS-CBCT: HyperSight cone beam computed tomography, MAR: Metal artifact reduction, HU: Hounsfield unit, SD: Standard deviation

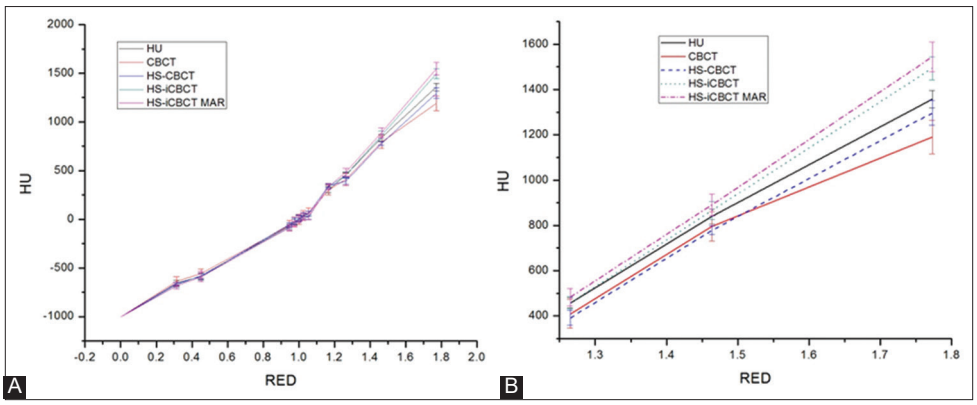

FIGURE 5. (A) Hounsfield unit relative electron density (HU-RED) part of the curve in the area RED < 1.8, (B) HU-RED curves for the area 1.2 ≤ RED < 1.8.

independently at two predefined RED intervals to account for density-dependent variations. Performance metrics for the low-to-intermediate density spectrum (RED < 1.2) are detailed in Table 4, providing a baseline for low-density soft tissue and lung equivalents. In contrast, statistical findings for the high-density region (1.2 ≤ RED < 1.8), which predominantly represents skeletal structures, are shown in Table 5.

The deviations between the measured doses at the LINAC (D_{meas}) and the corresponding doses calculated within the TPS (D_{cal}) at different anatomical locations of the CIRS Thorax phantom are shown in Figure 6a and b. These dosimetric comparisons, performed for VMAT plans derived from CT, HS-CBCT and HS-iCBCT datasets, specifically assess the impact of imaging modality on the accuracy of the calculations.

The results, obtained using a 6 MV photon beam, were systematically divided according to the calculation algorithm used, AAA or Acuros XB. Any differences observed were further compared with predefined clinical tolerance criteria to assess the feasibility of HS-CBCT or HS-iCBCT-based thoracic RT planning.

Analysis of 60 individual measurement points (10 phantom measurement positions, 3 imaging modalities: CT, HS-CBCT and HS-iCBCT, and 2 calculation algorithms, we get a total of 60 measurement positions) revealed a high degree of agreement between measured and calculated dose.

TABLE 5. Statistical indices of agreement and Pearson correlation coefficients between the reference CT and alternative imaging modalities (CBCT, HS-CBCT, HS-iCBCT, and HS-iCBCT MAR) within the 1.2≤RED<1.8 interval

Imaging	Δ_{mean} (HU)	SD (HU)	RMSE (HU)	Max Δ_i	Pearson (*r*)	*p*-value
CBCT	−86.92	70.29	104.16	168.04	0.9967	0.052
HS-CBCT	−62.82	3.45	62.88	66.73	0.9999	0.035
HS-iCBCT	54.22	72.16	80.07	136.04	0.9994	0.021
HS-iCBCT MAR	88.08	86.69	113.00	186.96	0.9990	0.028

RED: Relative electron density, CT: Computed tomography, CBCT: Cone beam computed tomography, HS-CBCT: HyperSight cone beam computed tomography, MAR: Metal artifact reduction, HU: Hounsfield unit, SD: Standard deviation

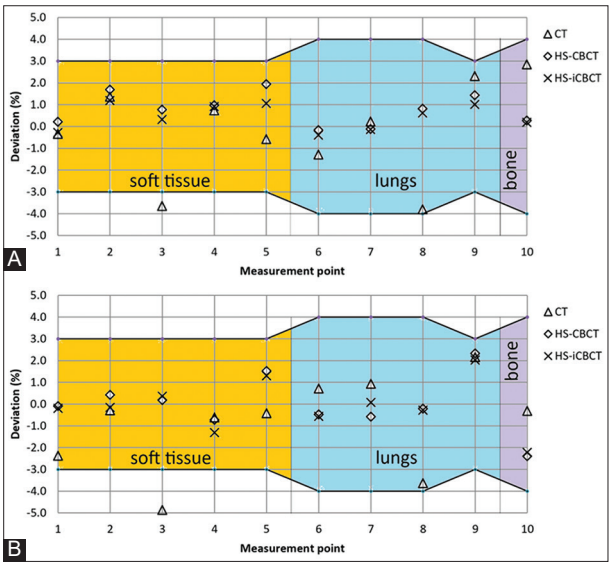

FIGURE 6. Dose differences between measured and treatment planning system-calculated values (based on computed tomography, HyperSight-cone beam computed tomography, and HS-iterative CBCT across all measurement points for the 6 MV volumetric modulated arc therapy plans: (A) Anisotropic analytical algorithm and (B) Acuros XB. Shaded areas represent a tolerance range of 3–4%.

Notably, only a single data point (1.7%) exhibited a discrepancy exceeding the 4% threshold, falling within the 4–5% range (Figure 6b). Minor deviations, situated between 3% and 4%, were observed at 3 measurement locations (5%). Regarding the directionality of the errors, the dose calculated by the TPS was lower than the experimentally measured dose in 28 instances (46.7%), whereas an overestimation by the TPS was recorded in 32 cases (53.3%), Figure 6a and b.

Statistical analysis (descriptive) of dose deviation measurements obtained in the CIRS Thorax phantom, based on 6 MV, VMAT plans, and using different imaging modalities (CT, HS-CBCT, and HS-iCBCT) and calculation algorithms (AAA or AcurosXB), is shown in Table 6.

DISCUSSION

The primary objective of this study was to assess the clinical viability of different imaging modalities by comparing their HU-RED conversion accuracy with a gold standard CT reference. Our findings support the hypothesis that, although all modalities maintain high overall correlation, their performance is inherently density dependent. The decision to split the analysis into two density regions (RED < 1.2 and 1.2 ≤ RED <1.8) was analytically necessary due to various physical interactions, such as beam hardening and photoelectric effect (absorption), which disproportionately affect CBCT image quality in high-Z (atomic number) materials (Table 3).

In the low-to-medium density spectrum (RED < 1.2), which represents the most clinically significant range for soft-tissue characterization, all evaluated modalities demonstrated very strong linear correlation with the CT baseline (r > 0.998, Table 4). Among the evaluated approaches, CBCT showed the smallest deviation from CT, with a mean difference of 4.81 HU and the lowest RMSE of 11.37 HU. The HS-CBCT method exhibited slightly larger deviations (RMSE = 14.80 HU), whereas HS-iCBCT and HS-iCBCT MAR produced slightly higher errors, with RMSE values of 19.15 HU and 17.50 HU, respectively. Despite these differences, the HU values obtained using all methods remained highly correlated with CT values and statistically significant (p < 0.001), indicating that all reconstruction approaches provide reliable HU estimation within the clinically relevant soft-tissue density range. The HU difference for all imaging is within ± 30 HU for the same RED values in relation to the CT curve (Figure 5a).

The results differ in the high-density region (1.2 ≤ RED < 1.8), where larger deviations were observed for all investigated methods (Table 5). This behavior is expected, as higher RED typically corresponds to materials such as bone, where CBCT reconstruction is more susceptible to beam hardening and absorption. In this region, HS-CBCT achieved the lowest RMSE (62.88 HU), suggesting improved stability compared to the standard CBCT reconstruction. In contrast, CBCT and HS-iCBCT MAR exhibited larger deviations, with RMSE values exceeding 100 HU. The MAR-corrected reconstruction tended to produce higher HU values compared to CT, which may indicate partial overcorrection of metal-induced artifacts.

Although Pearson correlation coefficients remained very high for all methods (r > 0.996), the statistical significance for CBCT in the high-density region was marginal (p = 0.052), primarily due to the limited number of available data points in this region (Figure 5b). Therefore, while the observed trends are informative, conclusions regarding the high-density region should be interpreted with caution.

Although all methods demonstrated near-perfect Pearson correlation, the actual agreement between HU-RED curves was primarily determined by bias and RMSE, since correlation alone does not account for systematic offsets between datasets. The HS-CBCT curve was the closest to the CT curve in that it shows the lowest RMSE (smallest overall deviation compared to the CT curve), minimal SD (the deviation is almost constant throughout the curve and the shape is almost identical to the CT curve) and Pearson correlation coefficients close to one, which indicates an almost identical shape of the curve (compared to the CT curve) with a stable systematic shift. All of the above results are in agreement with other studies (Kolarevic et al. (1) and Zurl et al. (14)).

TABLE 6. Descriptive statistics and Friedman non-parametric (χ^2) analysis comparing measured and TPS-calculated doses across different imaging modalities (CT, HS-CBCT and HS-iCBCT) and calculation algorithms (AAA and AcurosXB) for VMAT RT plan (6 MV)

Algorithm	Modality	Mean (%)	SD (%)	MAE (%)	χ^2	*p*
AAA	CT	−0.22	2.24	1.71	7.4	0.025
	HS-CBCT	0.78	0.74	0.84		
	HS-iCBCT	0.45	0.59	0.61		
Acuros XB	CT	0.01	1.28	0.89	1.4	0.497
	HS-CBCT	−0.87	2.15	1.63		
	HS-iCBCT	−0.1	1.2	0.85		

CT: Computed tomography, CBCT: Cone beam computed tomography, HS-CBCT: HyperSight cone beam computed tomography, MAR: Metal artifact reduction, HU: Hounsfield unit, SD: Standard deviation, VMAT: Volumetric modulated arc therapy, AAA: Anisotropic analytical algorithm, TPS: Treatment planning system

Overall, the results indicate that all imaging methods provide highly correlated HU values with CT, particularly in the clinically important soft-tissue density range. However, deviations increase for higher densities, emphasizing the importance of imaging method selection when accurate HU representation of dense materials is required.

The evaluation of absolute dose differences between LINAC measurements (D_{meas}) and TPS calculations (D_{cal}) for the 6 MV, VMAT plans demonstrated a high level of dosimetric consistency. Out of the entire dataset, only two measurements (3.3%) exceeded the predefined clinical agreement criteria. Interestingly, these outliers were localized within soft-tissue regions (Position 3, Figure 6a and b). In contrast, plans derived from HS-CBCT and HS-iCBCT imaging, utilizing their modality-specific calibration curves, maintained a high degree of accuracy, with a maximum recorded deviation of only 2.4% (observed at position 10, bone, using the HS-CBCT/AcurosXB).

Detailed analysis of the AAA algorithm (Table 6) identifies HS-iCBCT as the best imaging modality, characterized by the narrowest error distribution (SD = 0.59), the minimum mean absolute error, and superior overall accuracy. While HS-CBCT provided stable results, it exhibited slightly larger stochastic variations. A significant finding was that the largest dosimetric errors were indexed within the standard CT modality, which is traditionally considered the gold standard.

Iterative reconstruction in the HS-iCBCT modality likely improves image quality compared to standard HS-CBCT and conventional CBCT. Iterative algorithms reduce noise, reduce scatter artifacts, and improve HU homogeneity, which directly affects the accuracy of density conversion and dose calculation. More stable HU values lead to more accurate RED modeling in TPS.

The Friedman non-parametric (χ^2) analysis for the AAA algorithm revealed a statistically significant divergence ($p < 0.05$) among the three imaging modalities, necessitating the rejection of the null hypothesis regarding median equality. The consistently lower ranks achieved by HS-iCBCT further validate its status as the modality with the highest dosimetric fidelity.

Regarding the Acuros XB calculation engine, HS-CBCT displayed the highest degree of bias and variability. Conversely, HS-iCBCT demonstrated a better alignment with the CT reference in terms of both mean dose distribution and SD. The Friedman test for dependent samples ([χ^2] = 7.4, $p < 0.05$) confirmed that these differences are statistically significant when employing the AAA algorithm. The ranking system indicated that HS-CBCT systematically produced higher deviations, whereas HS-iCBCT and CT exhibited comparable, lower ranks, signifying enhanced precision and consistency.

These observations align with the research conducted by Kolarevic et al. (12) and Rutonjski et al. (15). Our data are further supported by the findings of Geise and McCullough (16), who postulated that an uncertainty of 4–10% in RED typically translates to a dose discrepancy of less than 2%, a threshold largely maintained in this study.

Finally, it is important to acknowledge that the constrained sample size (n = 10) represents a limitation of the current study, potentially impacting the statistical power and the broader generalizability of these results. However, the observed trends provide a compelling indication of the advanced dose calculation capabilities inherent in modern iCBCT reconstruction suites.

CONCLUSION

This study evaluated the agreement of several CBCT-based imaging methods and CT reference analysis by analyzing HU values as a function of RED. The results suggest that for the purposes of oART planning (VMAT, 6 MV), it is possible to use HS-CBCT and HS-iCBCT imaging in the area of RED < 1.8, which covers all types of tissues in patients. Future studies with a larger sample are recommended to confirm the obtained results.

FINANCIAL SUPPORT

The authors received no specific funding for this work.

DECLARATION OF INTEREST

The authors declare no conflict of interests.

REFERENCES

1. Kolarević G, Jaroš D, Pavičar B, Ignjić T, Kostovski A, Marošević G, et al. Computed tomography simulator conversion curve dependence on scan parameters and phantom dimension. J Health Sci. 2020;10(3):226-33.

   https://doi.org/10.17532/jhsci.2020.1085

2. Bogowicz M, Lustermans D, Trier Taasti V, Hazelaar C, Verhaegen F, Paiva Fonseca G, et al. Evaluation of a cone-beam computed tomography system calibrated for accurate radiotherapy dose calculation. Phys Imaging Radiat Oncol. 2024;29:e100566.

   https://doi.org/10.1016/j.phro.2024.100566

3. Gregg K, Arsenault T, Rezaei A, Kashani R, Henke L, Price A. Hounsfield Unit characterization and dose calculation on a C-arm LINAC with novel on-board cone-beam computed tomography feature and advanced reconstruction algorithms. J Appl Clin Med Phys. 2025;26(8):e70145.

   https://doi.org/10.1002/acm2.70145

4. Duan J, Pogue JA, Stanley DN, Shen S, Viscariello NN, Cardenas CE, et al. Assessing HyperSight iterative CBCT for dose calculation in online adaptive radiotherapy for pelvis and breast patients compared to synthetic CT. J Appl Clin Med Phys. 2025;26(5):e70038.

   https://doi.org/10.1002/acm2.70038

5. Sijtsema N, Penninkhof JJ, Van De Schoot AJ, Kunnen B, Sluijter JH, Van De Pol M, et al. Dose calculation accuracy of a new high-performance ring-gantry CBCT imaging system for prostate and lung cancer patients. Radiother Oncol. 2025;202:e110596.

   https://doi.org/10.1016/j.radonc.2024.110596

6. Varian Medical Systems. HyperSight- Imaging Solution Configuration. California: Varian Medical Systems; 2024.

7. Siemens Healthcare. SOMATOM go.Open Pro, user Guide. India: Siemens Healthcare; 2020.

8. Varian Medical Systems. TrueBeam-Technical Reference Guide-Imaging. California: Varian Medical Systems; 2023.

9. SunNuclear, A Mirion Medical Company. Advanced Electron Density Phantom, user Guide. United States: SunNuclear, A Mirion Medical Company; 2022.

10. SunNuclear, A Mirion Medical Company. IMRT Thorax Phantom (CIRS Model 002LFC), user Guide. United States: SunNuclear, a Mirion Medical Company; 2022.

11. Ebert MA, Lambert J, Greer PB. CT-ED conversion on a GE Lightspeed-RT scanner: Influence of scanner settings. Australas Phys Eng Sci Med. 2008;31(2):154-9.

    https://doi.org/10.1007/BF03178591

12. Kolarević G, Jaroš D, Marošević G, Ignjatić D, Mirjanić D. Dosimetric verification of clinical radiotherapy treatment planning system. Vojnosanit Pregl. 2022;79(2):115-24.

    https://doi.org/10.2298/VSP200411070K

13. Schiefer H, Fogliata A, Nicolai G, Cozy L, Selenga W, Born E, et al. The Swiss IMRT dosimetry intercomparison using a thorax phantom. Med Phys. 2010;37(8):4424-31.

    https://doi.org/10.1118/1.3460795

14. Zurl B, Tiefling R, Winkler P, Kindl K, Kapp KS. Hounsfield units variations: Impact on CT-density based conversion tables and their effects on dose distribution. Strahlenther Onkol. 2014;190:88-93.

    https://doi.org/10.1007/s00066-013-0464-5

15. Rutonjski L, Petrolia B, Baikal M, Teodorović M, Čudić O, Gershkevitsh E, et al. Dosimetric verification of radiotherapy treatment planning systems in Serbia: National audit. Radiat Oncol. 2012;7(1):155.

    https://doi.org/10.1186/1748-717X-7-155

16. Geise RA, McCullough EC. The use of CT scanners in megavoltage photon-beam therapy planning. Radiology. 1977;124(1):133-41.

    https://doi.org/10.1148/124.1.133